Periodic FDTD Analysis of Leaky-Wave Structures and Applications to the Analysis of Negative-Refractive-Index Leaky-Wave Antennas

Titos Kokkinos, *Student Member, IEEE*, Costas D. Sarris, *Member, IEEE*, and George V. Eleftheriades, *Fellow, IEEE*

***Abstract*—The determination of the attenuation constants of periodic leaky-wave structures via the finite-difference time-domain (FDTD) method has been pursued so far via the simulation of a number of unit cells that is large enough to guarantee the convergence of the computed value. On the other hand, Brillouin diagrams of periodic structures can be readily extracted via the simulation of a single unit cell, terminated in periodic boundary conditions. This paper demonstrates a methodology that enables the concurrent extraction of leaky-wave attenuation constants *and* Brillouin diagrams of periodic structures, through the FDTD simulation of a unit cell. The proposed methodology is first validated and then employed to model leaky-wave radiation from a two-dimensional negative-refractive-index transmission-line (NRI-TL) medium. Apart from evaluating the characteristics of forward and backward leaky-wave radiation from such a medium, a lumped-element macro-model, with element values determined from the FDTD simulation, is extracted. The FDTD analysis, combined with this equivalent circuit, is used to investigate theoretically the possibility of the NRI-TL medium, as a leaky-wave antenna, to achieve continuous scanning from backward to forward end-fire and broadside radiation.**

***Index Terms*—Complex propagation constants, finite-difference time-domain (FDTD) methods, leaky-wave antennas (LWAs), negative-refractive-index (NRI), periodic boundary conditions.**

I. Introduction

LEAKY-WAVE antennas (LWAs) have been extensively studied for several years, because of their comparative advantages, namely high directivity and frequency beam-scanning, but also the richness of the electromagnetic phenomena related to them. Recently, the study of leaky-waves in negative-refractive-index (NRI) metamaterial-based structures has indicated the possibility of designing novel types of one- and two-dimensional LWAs, thus adding a new direction of research to this area.

Theoretically studied by Veselago in [1], NRI media concurrently exhibit negative dielectric permittivity ($\epsilon < 0$) and magnetic permeability ($\mu < 0$) and, as a result, a negative refractive index ($n < 0$). The latter implies the support of backward-waves (characterized by antiparallel phase and group velocities or the formation of a left-handed triplet by the wave vector $\overline{k}$, the electric field vector $\overline{E}$, and the magnetic field $\overline{H}$) by these media. Recent realizations of NRI "metamaterials." in the form of composite periodic structures of negative effective parameters, have enabled the experimental investigation of their unconventional properties and salient features. While the split-ring resonator and thin-wire structure of [2] offered the first demonstration of an NRI medium, a loaded transmission-line (TL) approach provided a planar and broad-band alternative implementation [3]–[6].

One of the several loaded NRI-TL metamaterial-based applications that emerged in the literature is their use for the design of one-dimensional (1-D) LWAs radiating in the backward end-fire direction [7], [8] or having a beam-scanning capability from backward to forward end-fire [9], [10]. Furthermore, two-dimensional (2-D) LWAs, based on loaded NRI-TL grids, have been studied in [11]–[13]. Inspection of the dispersion diagram of the 2-D loaded NRI-TL metamaterial grid of [4] (shown in Fig. 1) reveals the existence of a fast wave region (where the phase constant β of the structure is smaller than the free space propagation constant k_0). Within this region, first backward and then forward waves are supported. Then, the phase-matching condition at the interface between the dielectric substrate of the metamaterial and air enforces the emergence of a leaky-wave beam at an angle

$$\theta_m = \sin^{-1}\left(\frac{\beta}{k_0}\right) \tag{1}$$

implying the operation of the metamaterial grid as a 2-D LWA. Furthermore, the transition of β from negative to positive values suggests that the angle of emergence of the leaky waves can theoretically vary from $-\pi/2$ to $\pi/2$.

The aforementioned structure is the motivating application for this paper's research into the full-wave analysis of LWAs via the finite-difference time-domain (FDTD) technique. A particular question of interest that stems from the survey of previous work in this area is whether it is possible to extract the attenuation constant of leaky-wave periodic structures from the FDTD analysis of their unit cell. This question becomes intriguing by the fact that the translation of Floquet's boundary conditions from the frequency domain (where they are naturally cast) to

Manuscript received October 30, 2005; revised December 23, 2005. This work was supported by the Natural Sciences and Engineering Research Council of Canada under a Discovery Grant and a Strategic Grant.

T. Kokkinos was with the Edward S. Rogers Sr. Department of Electrical and Computer Engineering, University of Toronto, Toronto, ON, Canada M5S 3G4. He is now with the Wireless Communications Research Group, Loughborough University, Leicestershire LE11 3TU, U.K.

C. D. Sarris and G. V. Eleftheriades are with the Edward S. Rogers Sr. Department of Electrical and Computer Engineering, University of Toronto, Toronto, ON, Canada M5S 3G4 (e-mail: cds@waves.toronto.edu).

Digital Object Identifier 10.1109/TMTT.2006.871367

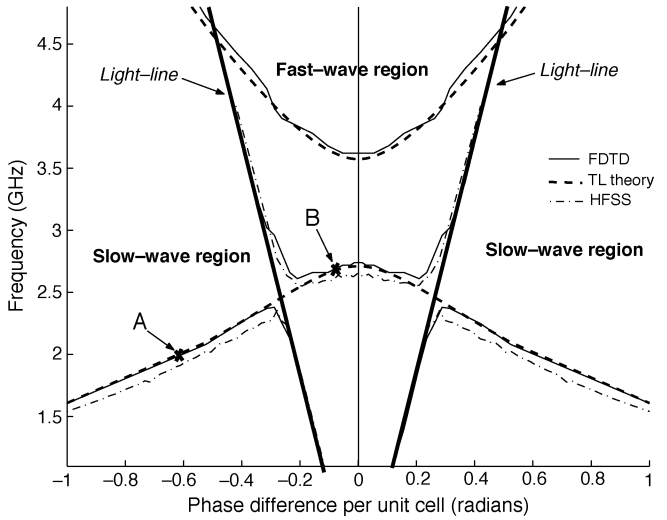

Fig. 1. Brillouin diagram of the loaded NRI-TL unit cell of [22], extracted through the periodic FDTD analysis of [21], around the $\beta = 0$-region. The results, for both the slow and fast waves, are in agreement with those extracted through the TL theory-based analysis of [23] and Ansoft's HFSS.

the time domain is invariably pursued by fixing the phase difference between the field components at the boundaries of a unit cell to a real number and determining the resonant frequencies of fields sampled within the cell [14]–[17]. On the contrary, previous computations of attenuation constants of LWAs were exclusively made by simulating a relatively large number of unit cells, terminated into regular absorbing boundary conditions, until the value of the convergence of the attenuation constant was achieved [29].

This paper builds on previous work by the authors [18], [19] to demonstrate a methodology that allows the extraction of *complex* propagation constants from an FDTD simulation of a unit cell of a leaky-wave structure terminated in periodic boundary conditions. The proposed technique is initially validated and then applied to the modeling of leaky-wave radiation from the loaded NRI-TL grid of [4]. In particular, the frequency dependence of the attenuation constant of the forward and backward fast waves in the structure is determined. This dependence is considered when the stopband indicated in the dispersion diagram of Fig. 1 at $\beta = 0$ is open *and* in the limiting case of that being closed. Finally, the FDTD simulations allow for the extraction of a lumped-element equivalent circuit that captures the physical behavior of the structure and illuminates some of its qualitative features.

II. Leaky-Wave Structure Modeling in Periodic FDTD Implementations

This section is aimed at investigating the possibility to extract complex propagation constants of leaky-wave periodic structures via the FDTD analysis of their unit cell. To that end, the implementation of periodic boundary conditions (PBCs) in FDTD is briefly revisited and carefully inspected.

Consider a 2-D periodic structure of periodicities d_x and d_y in the x and y directions, respectively. Then, its direct lattice vector is $\overline{p} = d_x\hat{x} + d_y\hat{y}$. Letting the reciprocal lattice wave vector of the structure be $\overline{\beta} = \beta_x\hat{x} + \beta_y\hat{y}$, Floquet's theorem, in the frequency domain, can be cast in the form of the following equations:

$$\tilde{\overline{E}}(\overline{r} + \overline{p}) = \tilde{\overline{E}}(\overline{r})e^{-j\overline{k}\cdot\overline{p}} \tag{2}$$

$$\tilde{\overline{H}}(\overline{r} + \overline{p}) = \tilde{\overline{H}}(\overline{r})e^{-j\overline{k}\cdot\overline{p}} \tag{3}$$

where $\tilde{\overline{E}}$ and $\tilde{\overline{H}}$ are phasors of the electric and magnetic fields, respectively, while $\overline{k} = (\beta_x\hat{x} + \beta_y\hat{y}) - j(\alpha_x\hat{x} + \alpha_y\hat{y})$ is a complex propagation constant, where $\overline{\alpha} = (\alpha_x\hat{x} + \alpha_y\hat{y})$ is the corresponding attenuation constant vector.

In the past, the translation of (2) and (3) from the frequency to the time domain and their incorporation into the FDTD update equations was negotiated for the case of purely real propagation constants [20]. In general, the direct implementation of these equations in an FDTD framework is impossible, since it results in update equations involving future (unknown) field values. In order to circumvent this problem, several techniques have been proposed. As mentioned in the Introduction, their common starting point is to fix the wave-vector components to real values and deduce the frequencies to which they correspond via the computation of the resonant frequencies of the sampled fields. A question that is naturally posed is whether such a methodology would preclude the determination of any attenuation constants involved, limiting the applicability of these techniques only to cases where $\alpha_x = \alpha_y = 0$.

In [21], the authors applied the sine–cosine method of [14] in order to perform the dispersion analysis of the NRI medium of [4]. The part of the dispersion diagram corresponding to axial propagation (the $\Gamma - X$-part of the Brillouin zone) is shown in Fig. 1. The PBCs used for this diagram are: $\beta_x d_x = \beta d$, with $-1 \leq \beta d \leq 1$ (in radians) and $\beta_y d_y = 0$. Note that, although the structure is 2-D, only axial propagation is considered throughout this paper, allowing for the unambiguous use, henceforth, of $\beta = \beta_x$ and $d = d_x$. The diagram includes both slow and fast waves, whose resonant frequencies were computed in a unified way via the sine–cosine method. However, an inspection of the associated field resonances for slow and fast waves indicates an important difference that is illustrated through the following two examples. First, when the phase difference corresponding to point A of Fig. 1, with $\beta d = -0.6$ rad, is enforced between the x-directed boundaries of a unit cell, then the vertical electric field inside the structure exhibits the nondecaying resonance pattern shown in Fig. 2. On the other hand, moving the point of interest inside the fast-wave region of the structure, when the phase difference corresponding to point B of Fig. 1, with $\beta d = -0.07$ rad, is enforced, the field pattern exhibits a decaying resonance, as shown in Fig. 3. In both cases, the field initially follows the source excitation (a Gabor pulse). When the excitation fades away, the mode that corresponds to the enforced β is established within the cell. In the absence of any ohmic or dielectric losses inside the unit cell, one can only interpret this decaying resonance as evidence of radiation, successfully accounted for by the FDTD method, even though PBCs without any explicit enforcement of an attenuation constant are employed.

These numerical observations have an important implication regarding the nature of methods that implement PBCs in FDTD,

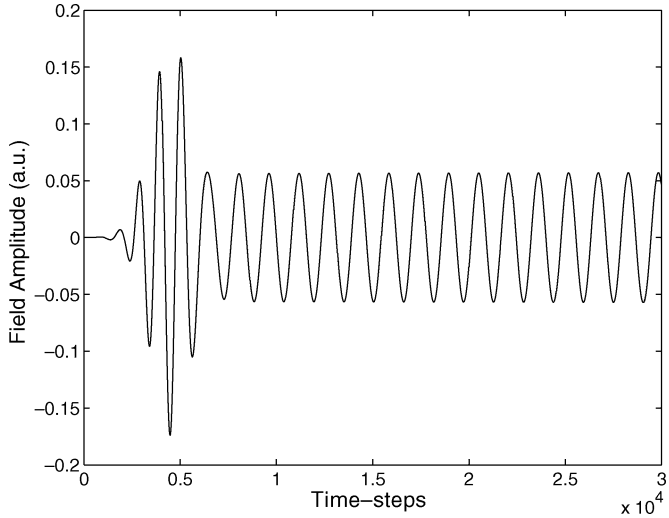

Fig. 2. Time-domain evolution of the vertical electrical field of a slow-wave mode within the unit cell of the loaded NRI-TL metamaterial structure (terminated with the PBCs $\beta_x d_x = -0.6$ rad, $\beta_y d_y = 0$ rad).

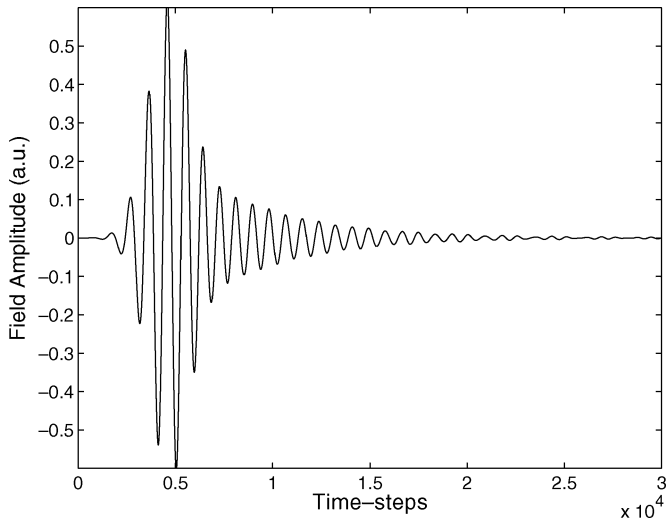

Fig. 3. Time-domain evolution of the vertical electrical field of a fast-wave mode within the unit cell of the loaded NRI-TL metamaterial structure (terminated with the PBCs $\beta_x d_x = -0.07$ rad, $\beta_y d_y = 0$ rad).

such as the split-field and the sine–cosine methods. When the propagation constant β along the x axis is fixed to a certain real value, the condition that is numerically realized is NOT

$$\tilde{\overline{E}}(\overline{r} + d\hat{x}) = \tilde{\overline{E}}(\overline{r}) e^{-j\beta d}$$

since the latter would not allow for a decaying resonance, but

$$\angle \tilde{\overline{E}}(\overline{r} + d\hat{x}) - \angle \tilde{\overline{E}}(\overline{r}) = -\beta d. \tag{4}$$

.

In order to support the validity of this statement, the field update procedure in a periodic FDTD code is analyzed. For simplicity, let us consider the one-dimensional (1-D) domain of a unit cell (Fig. 4), which corresponds to a TEM-wave case. Electric field nodes are positioned on the periodic boundaries.

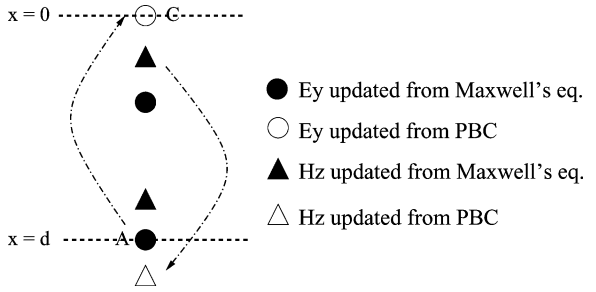

Fig. 4. Updates of field components at the boundaries of the unit cell of a 1-D periodic structure through the application of PBCs and FDTD update equations.

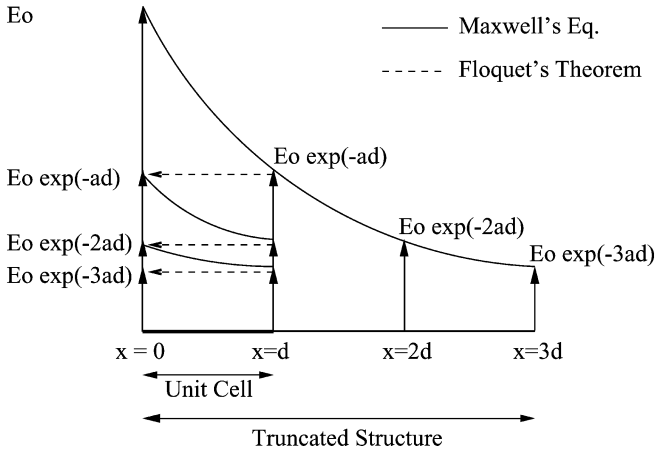

Fig. 5. Evolution of the electric field amplitude within a single unit cell of a lossy structure (with PBCs enforced along the axis of periodicity) compared with the one in three cells of the corresponding infinite periodic structure.

Then, the updates proceed as follows. Solving Maxwell's equations, one can update E_y^A on node A, since its neighboring H_z^A is known from H_z^C through the PBC (magnetic field updates are complete, once the electric field updates start). Then, E_y^A is used to update E_y^C, which is necessary for the magnetic field updates that follow. Note that the direction of this update is forward (a node at $x = 0$ is used to update a node at $x = d$). Once the magnetic updates proceed, H_z^C is updated by Maxwell's equations, and its value is transferred to H_z^A and so on. Note that the direction of this update is backward (a node at $x = d - \Delta x/2$ is used to update a node at $x = -\Delta x/2$). Therefore, if the modal field that FDTD solves for is leaky, then the spatial field decay cycle is *not* interrupted upon the enforcement of the PBCs, precisely because of this leap-frog sequence of boundary updates. On the contrary, this cycle is extended and taken care of through the implicit application of the boundary conditions in FDTD and the solution of Maxwell's equations, which produce a field decay in space at a rate set by the attenuation coefficient. This is the reason that (4) is the condition actually implemented in a periodic FDTD technique. The way a leaky mode is accounted for by a periodic FDTD technique is clearly depicted in Fig. 5, where the spatial evolution of the field amplitude within a single unit cell is shown, along with the field amplitude in three cells of the infinite periodic structure, as a function of space. The key observation is that the spatial attenuation of fields in an infinite periodic structure is reproduced within the unit cell, during the FDTD time-marching procedure, allowing for the calculation of

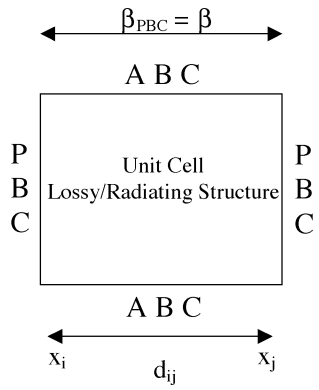

Fig. 6. Field sampling points within a unit cell of a periodic structure for the calculation of the complex propagation constant with (5).

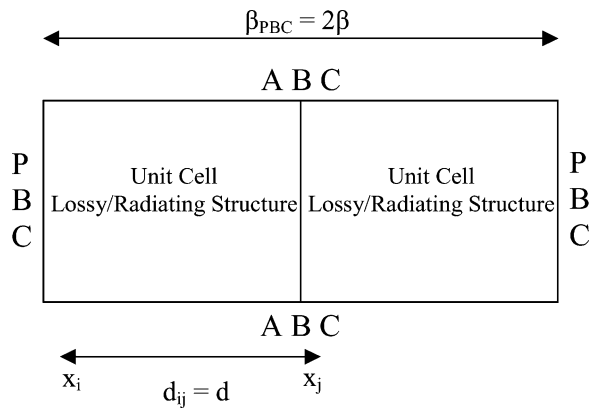

Fig. 7. Field sampling points one spatial period apart from each other for the calculation of the complex propagation constant with (5).

its rate (which is the attenuation constant sought for). It is finally noted that one would arrive at the same conclusion no matter how the field nodes had been arranged in the domain of Fig. 4.

The outstanding question of *how* the attenuation constant of a leaky wave can be computed is addressed in the following section.

III. Methodology for the Periodic FDTD Analysis of Leaky-Wave Structures

A. Attenuation Constant Calculation

For the determination of the attenuation constant α in a periodic leaky-wave structure, a standard technique employed for the calculation of attenuation constants in lossy/radiating (nonperiodic) guiding structures [25] is applied. However, the domain of application of this approach is now the unit cell of a periodic structure and is terminated at PBCs that enforce, per the analysis of the previous section, the phase constant of the waves excited in the cell to that of a fast wave in the structure. In particular, if $w(t,x)$, which is the waveform of either an electric or a magnetic field component, is sampled at two points x_i and x_j (Fig. 6) along the axis of periodicity, then the complex propagation constant $k = k_x$ can be deduced as

$$k(\omega) = j\frac{1}{x_j - x_i}\log\frac{\mathcal{F}[w(t,x_i)]}{\mathcal{F}[w(t,x_j)]} \tag{5}$$

where $\mathcal{F}$ denotes a Fourier transform. Evidently, the real part of the complex propagation constant k in (5) has to be the same as the PBC-enforced phase constant β of the fast wave ($\beta = \Re(k)$). Therefore, the real part of (5) offers redundant information, which is useful only as a confirmation that the correct phase constant has been implemented. The imaginary part of (5) provides the attenuation constant α ($\alpha = \Im(k)$) of the simulated mode.

The choice of the points x_i and x_j in (5) deserves special attention as a consequence of the fact that the computational domain is the unit cell of a periodic structure and (5) is supposed to provide an *effective* complex propagation constant per unit cell. Therefore, the distance between these points should be as close to one period d as possible. If Δx is the cell size along the axis of periodicity, the maximum distance between two nonboundary points within the domain of one unit cell is equal to $d - 2\Delta x$. Evidently, this distance tends to d as the cell size Δx tends to zero. Alternatively, one can extend the computational domain to include two unit cells, enforcing twice the phase difference per unit cell at its boundaries (Fig. 7). Then, the choice of two points *exactly* one period apart is straightforward, and we dispense with the relevant limitation on the cell size. This approach leads to a significant reduction in the computational cost of periodic structure modeling without compromising accuracy.

Finally, the determination of the real part of the propagation constant as a function of frequency is pursued in the same way as in [21].

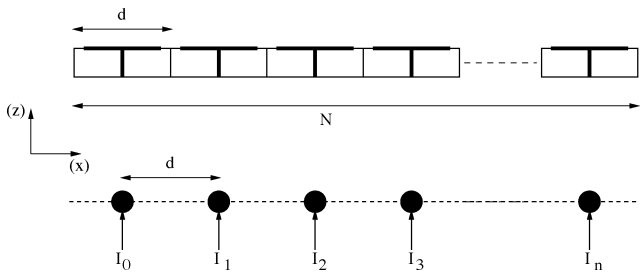

Fig. 8. One-dimensional leaky-wave structure treated as a phased array (under the condition $d \ll \lambda$).

B. Radiation Pattern Extraction

Since the modeling of NRI-based LWAs is the motivating application of this study, the computation of radiation patterns with the proposed FDTD analysis is also negotiated. Noting that the unit cells of such structures are electrically small (the unit cells of the NRI grid of [4] are less than one-tenth of a wavelength), the phased-array approach invoked in [26] and [27] is applicable here as well. Under this approach, each cell of the antenna is assumed to be a point source, fed with a current of the form $I_n = I_o e^{-n\alpha d} e^{-j\varphi_n}$ (Fig. 8), where $\varphi_n = n\beta d$. Then, the radiation pattern of the antenna is calculated using the following expression for the corresponding normalized array factor:

$$AF = \sum_{n=0}^{N-1} e^{-n\alpha d} e^{jn\left(\frac{2\pi d\cos\gamma}{\lambda} - \beta d\right)} \tag{6}$$

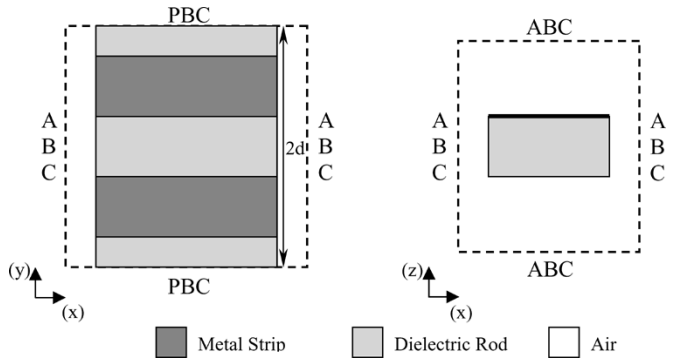

Fig. 9. Computational domain for the periodic FDTD analysis of the metal-strip-loaded dielectric LWA of [28] and [29].

where λ is the wavelength of operation and γ is the angle from the axis of propagation. Our analysis derives the $\alpha(\omega)$, $\beta(\omega)$ of an infinitely periodic structure, while (6) is evaluated for a finite array. The number of elements N in (6) is appropriately chosen for the computed radiation pattern to converge (typically, $N \geq 50$ is sufficient).

IV. Numerical Results: Validation

A. Metal-Strip-Loaded Dielectric LWA

In this section, the proposed method is validated by comparison to previously published results. A case study of interest is the metal-strip-loaded dielectric LWA, initially proposed by Klohn *et al.* [28] and then analyzed in [29]. The latter reference follows the standard FDTD methodology of simulating a truncated periodic structure composed of 29 unit cells, in order to approximate the complex propagation constant of the infinite periodic one at an operating frequency of 80 GHz. On the contrary, this study uses the compact computational domain of Fig. 9. The dimensions involved with this geometry are as follows: the spatial periodicity d of the structure (along the y direction) is 2.5 mm. The width and the height of the dielectric substrate supporting the metal strips are $w = 3$ mm and $h = 1.5747$ mm, respectively, and the dielectric constant of the substrate is $\epsilon_r = 2.33$. The width of the metal strips is $0.5d$. The strips are modeled as perfect electric conductors. Two unit cells are included along the y direction, while the sampling points for the electric field are chosen to be exactly one spatial period apart. In all other directions, the antenna is interfaced with free space, which is terminated in Mur's first-order absorbing boundary conditions. The absorbing boundaries are 15 cells away from the air–dielectric interfaces. In total, a mesh of $N_x \times N_y \times N_z = 20 \times 40 \times 33$ Yee's cells is used. The computational domain is excited with a Gabor pulse of a bandwidth of 10 GHz around the operating frequency. This pulse excites an electric field which is polarized parallel to the metal strips and has a spatial profile of the form $F(x,z) = \sin(\pi x/w)\sin(\pi z/h)$, corresponding to the TE_{11} mode.

In Fig. 10, the time-domain evolution of the electric field at a sampling point inside the dielectric substrate is shown for the case $\beta/k_o = -0.218$. This value corresponds to a leaky-wave mode supported at 80 GHz. During the transient stage of the first

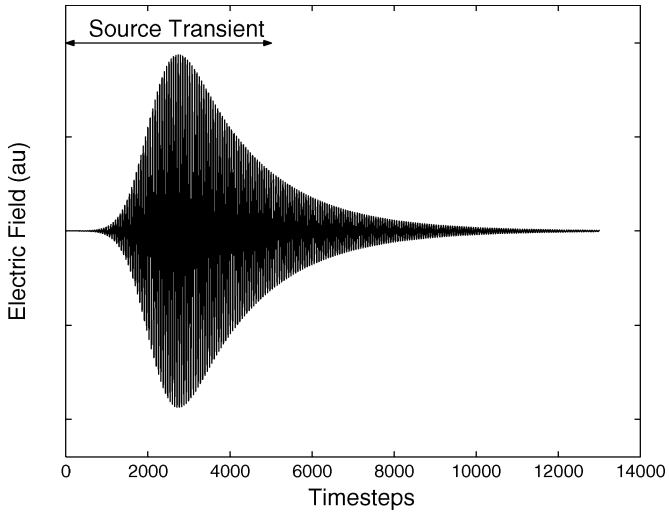

Fig. 10. Time-domain evolution of the electric field within the unit cell of the metal-strip-loaded dielectric LWA of [28] and [29] for $\beta/k_o = -0.218$ (fast-wave mode).

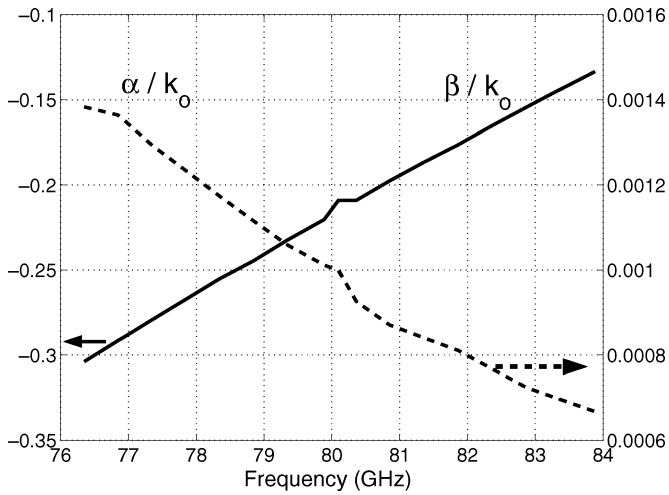

Fig. 11. Complex propagation constants for the metal-strip-loaded dielectric LWA of [28] and [29] calculated with the proposed method (periodic FDTD).

5000 time steps, the signal essentially follows the source excitation. At this stage, both evanescent and propagating modes exist in the structure. Eventually, the simulation reaches the steady state, during which the frequency of the supported mode becomes dominant and a traveling wave propagates in the dielectric. During this steady-state period, the amplitude of the electric field decreases exponentially with time.

In Fig. 11, the FDTD results for the real and imaginary parts of the complex propagation constant are presented. These results are in excellent agreement with those of [29]. Moreover, in Fig. 12, the attenuation constant α obtained from the periodic FDTD analysis is compared with the values of α obtained by simulating finite versions of this LWA, with a variable number of unit cells. For the latter simulations, Ansoft's HFSS is used. It is observed that α converges to the value of the infinite structure, when at least seven unit cells are employed. On the other hand, the proposed technique relies on PBCs, thus saving cells within the working volume and execution time.

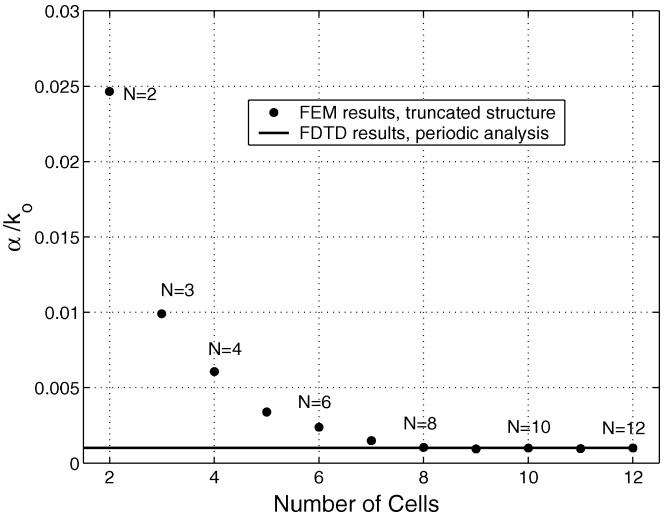

Fig. 12. Convergence of the attenuation constant of the metal-strip-loaded dielectric LWA of [28] and [29], with the number of the simulated unit cells, when the antenna is analyzed as a truncated structure (with Ansoft's HFSS), compared with the proposed method (periodic FDTD).

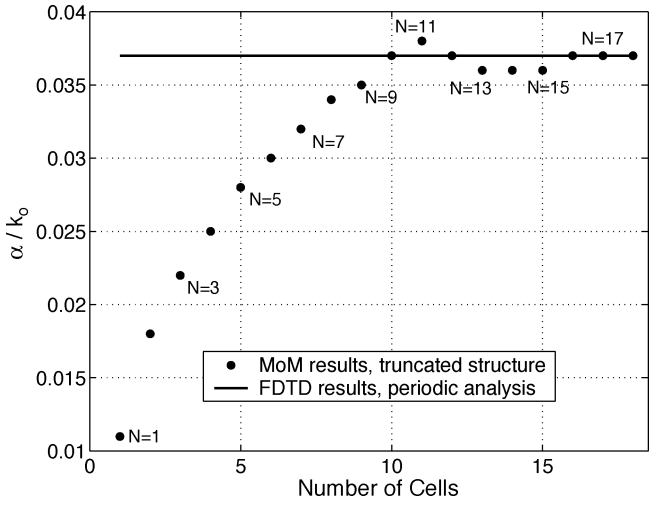

Fig. 14. Convergence of the attenuation constant (at 30 GHz) of the leaky CPW-based slot antenna array of [30], with the number of the simulated unit cells, when the antenna is analyzed as a truncated structure (with Agilent's Momentum), compared with the proposed method (periodic FDTD).

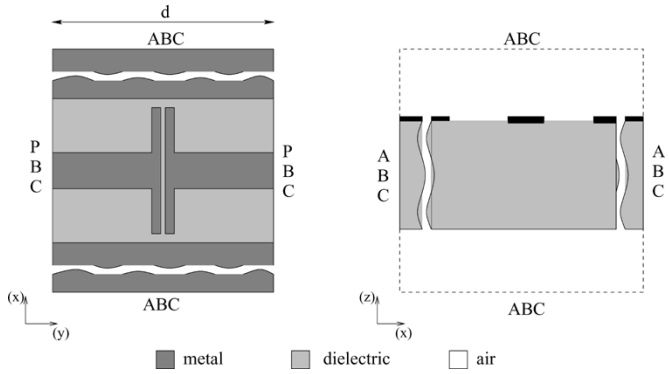

Fig. 13. Computational domain for the periodic FDTD analysis of the leaky CPW-based slot antenna array of [30].

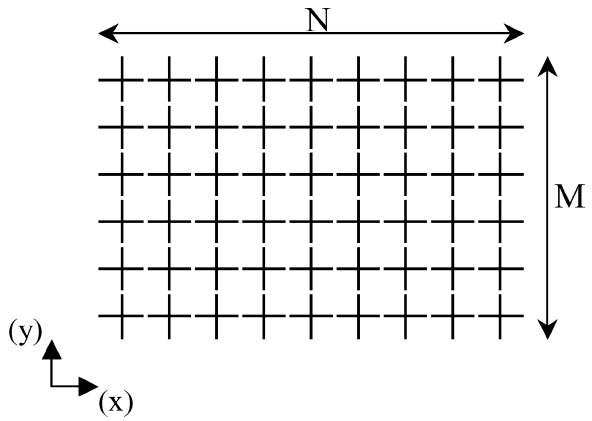

Fig. 15. Top view of the 2-D loaded NRI-TL grid of [4].

B. Leaky Coplanar-Waveguide-Based Slot Antenna Array

The second validation case for the proposed technique is the analysis of the leaky coplanar-waveguide (CPW)-based slot antenna array of [30]. The computational domain used to simulate the antenna is shown in Fig. 13. The operating frequency is 30 GHz. Following the standard analysis procedure of this paper, the real part of the propagation constant of the supported leaky-wave mode at 30 GHz is found to be $\beta/k_o = 0.72$, while the imaginary part of the propagation constant is $\alpha/k_o = 0.037$. Both of these results are in agreement with the results of [30].

In Fig. 14, the FDTD-determined attenuation constant of the infinite array is compared to results for finite versions of the structure, presented in [30]. The latter were extracted by Agilent's Momentum, which is a method-of-moments (MoM)-based package. The convergence of the attenuation constant of the finite arrays to that of the infinite array is rather slow. In fact, about 16 cells are needed for the value of the extracted α to converge. In comparison, the proposed FDTD technique utilized just one unit cell of the structure. In this case, the use of two unit cells is unnecessary, since the mesh is already dense because of the presence of the slot inside the unit cell. Therefore, the condition that the distance between the grid points employed for the implementation of (5) be close to one period is naturally satisfied.

V. Numerical Results: Periodic FDTD Analysis of 2-D Loaded NRI-TL Metamaterial-Based LWAs

A. Open Stopband Case

The numerical tool developed and validated above is now applied to the motivating case of this study, namely, the periodic FDTD analysis of the 2-D loaded NRI-TL grid of [4], operating in its fast-wave region as an LWA. In the following, the modeling of this antenna is pursued via this study's periodic FDTD approach and the sampling scheme of Fig. 7. Numerical results regarding the complex propagation constant of the leaky waves and their radiation pattern are reported.

A top view of the structure, indicating the series capacitively-loaded TL strips (complemented by shunt inductors), is given in Fig. 15. The structure is left edge-fed by an array of in-phase sources parallel to the y axis. As a result, wave propagation along the x axis is generated, while the E-plane of the resulting LWA is perpendicular to the plane of the structure and the y axis. In the following simulations, the values of the loading lumped

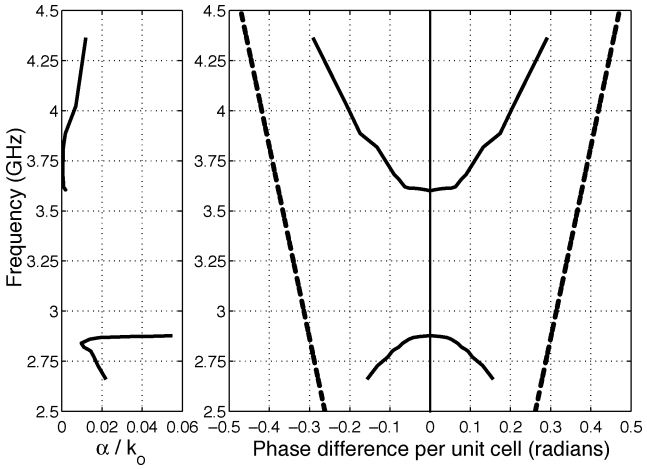

Fig. 16. Complex propagation constants of the radiating modes supported by the 2-D loaded NRI-TL grid of [4], operating as an LWA, with loading elements $L_0 = 5.6$ nH and $C_0 = 1.0$ pF (open stopband case). On the left, the attenuation constant is plotted as a function of frequency. On the right, the phase constant is plotted as a function of frequency (dashed line indicates the light line $\beta = k_0$).

elements are chosen to be $C_0 = 1.0$ pF and $L_0 = 5.6$ nH and the characteristic impedance of the host TL is set to $Z_0 = 141\ \Omega$.

In Fig. 16, the phase and attenuation constant of the simulated NRI medium are plotted as a function of frequency, inside the fast-wave region of the structure. The lower branch of each diagram corresponds to backward waves, while the upper branch corresponds to forward ones. The two branches are separated by a stopband forming around the $\beta = 0$-point. The waves follow the left-lower (backward-wave) branch, then encounter the stopband, and afterward continue on the right-upper (forward-wave) branch. These branches exhibit a positive group velocity (evidenced by the slope of the dispersion curve in Fig. 16), which implies a power flow from the source toward the semi-infinite space to its right.

The plots include only radiating modes. Note that these modes do not occur right after the boundary of the slow-to-fast wave region that is defined by the light line. As discussed in [21], the fast backward-wave modes close to the light line couple to the nonradiating surface waves, which follow the light line and hence do not contribute to leakage effects. The same argument holds for the fast forward-wave modes close to the light line.

The attenuation and phase constants depicted in Fig. 16 can be employed to calculate the angle of emergence of the leaky-wave beam from (1). Since β assumes negative and positive values, this angle assumes both negative and positive values, indicating the capability of the antenna to radiate both backward and forward. In particular, backward-wave radiation starts at -38° at the frequency of 2.6 GHz. The main beam is scanned continuously with frequency toward broadside. Just before broadside, the stopband is developed and, subsequently, leaky-wave radiation is interrupted from 2.8 to 3.6 GHz. At 3.6 GHz, the forward fast-wave band emerges. In this band, the radiated beam is scanned from broadside toward forward end-fire, until the angle of $+43^\circ$ is achieved at 4.36 GHz. As for the attenuation constant, its value decreases from backward end-fire toward broadside and suddenly increases just before broadside, due to the formation of the stopband around $\beta = 0$ (Fig. 16). In the forward radiation region, the attenuation increases from almost broadside toward forward end-fire.

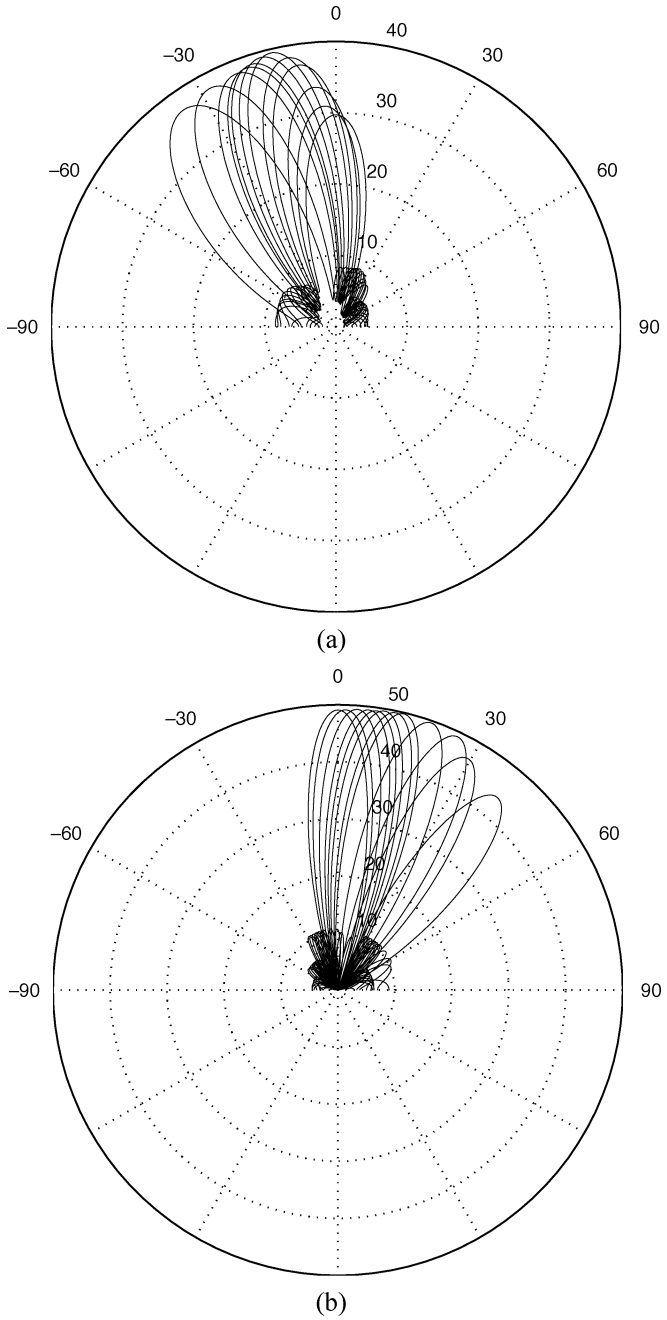

Fig. 17. Radiation patterns (E-plane) of the loaded NRI-TL grid of [4], operating as an LWA, with loading elements $L_0 = 5.6$ nH and $C_0 = 1.0$ pF (open stopband case). The frequency scanning range extends from 2.6 to 4.36 GHz. (a) Backward-radiation patterns. (b) Forward-radiation patterns.

Leaky-wave radiation patterns, computed with the phased-array approach (6), are shown in Fig. 17. In order to guarantee the convergence of these patterns, $N = 50$ elements were used. The changes in the maxima of these radiation patterns are inversely proportional to the changes in the attenuation constant of Fig. 16; the maxima of the backward radiated beams increase from backward end-fire toward broadside and decrease just before broadside, due to the sudden increase of the attenuation

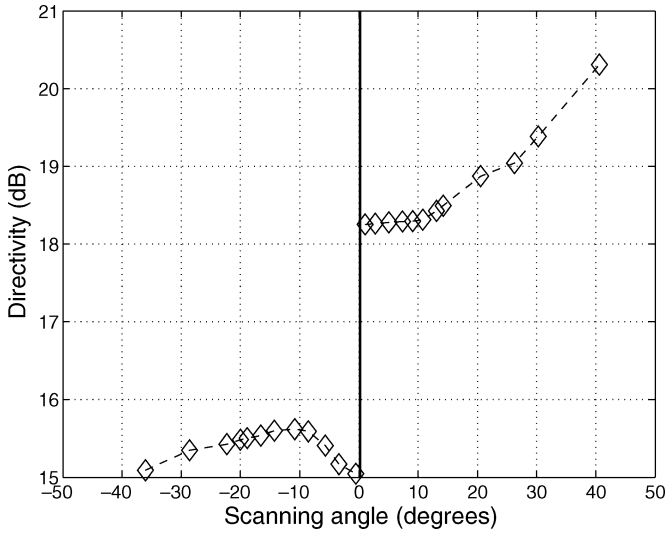

Fig. 18. Directivity of the loaded NRI-TL grid of [4], operating as an LWA, with loading elements $L_0 = 5.6$ nH and $C_0 = 1.0$ pF (open stopband case).

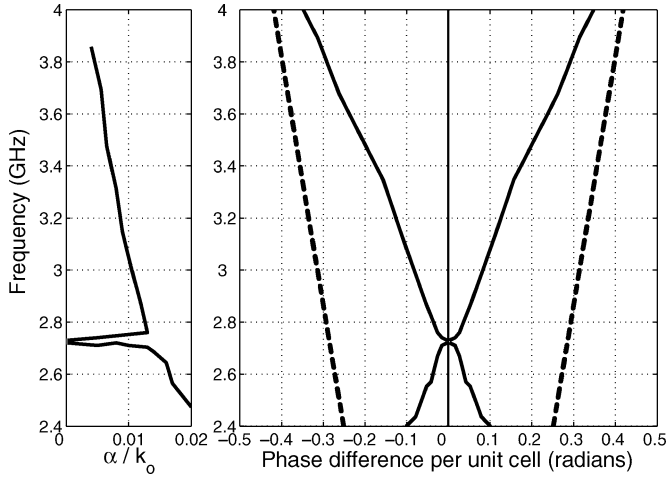

Fig. 19. Complex propagation constants of the radiating modes supported by the loaded NRI-TL grid of [4], operating as an LWA, with loading elements $L_0 = 10.0$ nH and $C_0 = 1.0$ pF (closed stopband). On the left, the attenuation constant is plotted as a function of frequency. On the right, the phase constant is plotted as a function of frequency (dashed line indicates the light line $\beta = k_0$).

constant. In the forward radiation region, these maxima decrease from broadside to forward end-fire. Finally, the directivity of this LWA, as a function of frequency, is plotted in Fig. 18. It is worth mentioning that the directivity of the antenna for the forward radiation region is also larger than the directivity of the antenna for the backward radiation region and increases from broadside to forward end-fire.

B. Closed Stopband Case

The analysis presented above is repeated for a grid loaded by shunt inductors of value $L_0 = 10.0$ nH instead of $L_0 = 5.6$ nH. The loading capacitors remain the same as before. For this inductive loading, the condition for a closed stopband [4], [34]

$$\frac{Z_0}{\sqrt{2}} = \sqrt{\frac{L_0}{C_0}} \tag{7}$$

is met. Indeed, Fig. 19 presents the results of the relevant dispersion analysis, indicating a closure of the stopband (whether this closure is exact will be discussed later) at $\beta = 0$. The frequency at which the backward-wave band meets the forward-wave band is $f_c = 2.72$ GHz. The associated values of the attenuation constant are shown on the left-hand side of Fig. 19. A comparison of the attenuation constants in Figs. 16 and 19 illuminates the differences between the open and closed stopband cases. In the latter case, α decreases from backward end-fire toward broadside, and, just before broadside, it drops suddenly to zero. In the forward radiation region, α increases for a small bandwidth until it starts decreasing toward forward end-fire. In summary, the attenuation constant decreases monotonically from backward end-fire to forward end-fire, apart from the region about the frequency f_c, where a sudden drop appears in the values of α.

Using the values of the complex propagation constant of Fig. 19 and (6), the radiation patterns are extracted (Fig. 20). The maxima of these patterns increase almost monotonically from backward end-fire to forward end-fire, apart from the region around broadside, where both the backward and forward radiation patterns achieve their maxima (just before and just after broadside). This observation agrees with the results of [32], which suggest that the radiated power of LWAs is maximized under the condition $|\beta| = |\alpha|$. Indeed, for the case of closed stopband, the complex propagation constant of the NRI-TL LWA satisfies the condition $|\alpha| \to |\beta|$, when $|\beta| \to 0$. The directivity related to these radiation patterns is shown in Fig. 21.

All of the aforementioned plots have *excluded* the point $\beta = 0$, which will be separately considered later in this paper, considering the two side limits $\beta \to 0^-, 0^+$.

VI. Equivalent Circuit Model for 2-D Loaded NRI-TL Metamaterial-Based LWAs

A. Determination of the Model Based on FDTD Results

The use of lumped-element models has accompanied the development of metamaterial devices, assisting the intuitive understanding of their properties and facilitating their design. For example, [31] demonstrated a simple equivalent circuit for the split-ring-resonator/thin-wire structure of [2]. For LWAs, both conventional and metamaterial-based, similar efforts have been reported [26], [27], [32]. In this section, the FDTD analysis of the 2-D loaded NRI-TL LWA is combined with an equivalent circuit topology proposed in [33] in order to extract a lumped element model that can reproduce all qualitative characteristics of the LWA, as registered by its full-wave analysis.

When no losses are to be accounted for, a 1-D NRI-TL metamaterial unit cell can be modeled using the equivalent circuit of Fig. 22, where L_0 and C_0 are the values of the loading elements and L_x and C_x correspond to the distributed inductance and capacitance of the hosting transmission line [4]. For a specific structure, the values of L_0, C_0, L_x, and C_x are well defined and, therefore, the propagation characteristics of NRI-TL metamaterial structures can be determined [4] using this circuit along

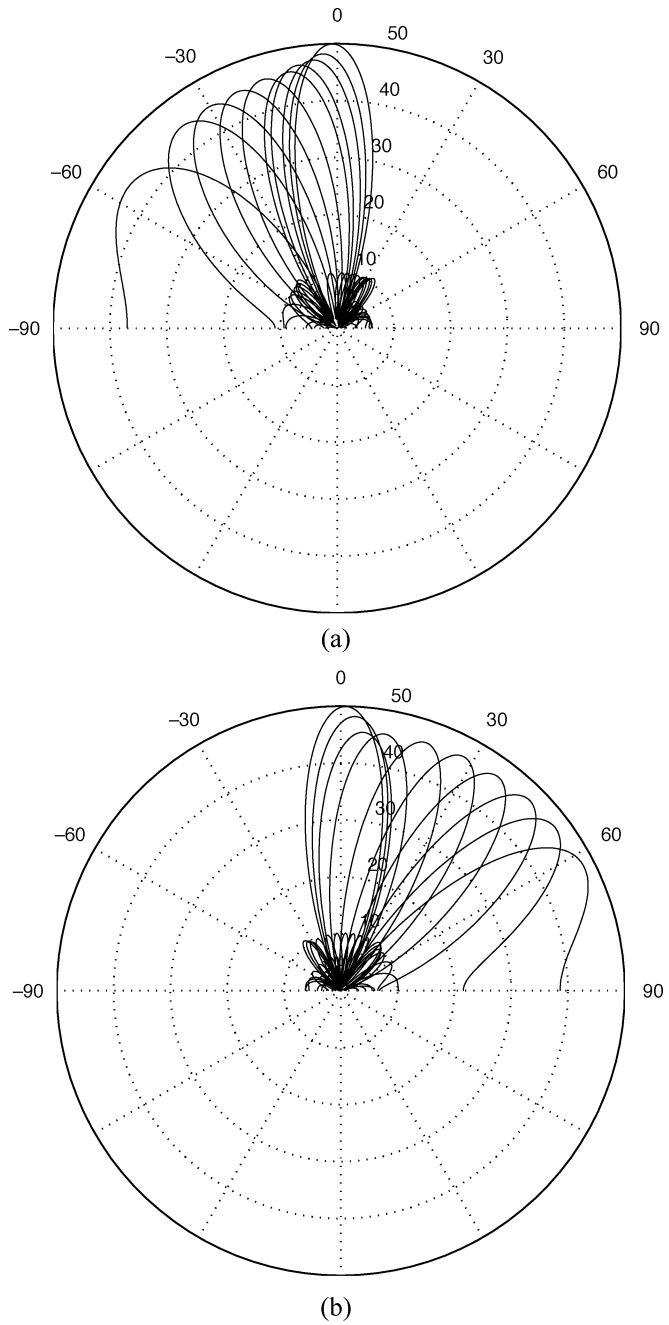

Fig. 20. Radiation patterns (E-plane) of the loaded NRI-TL grid of [4], operating as an LWA, with loading elements $L_0 = 10.0$ nH and $C_0 = 1.0$ pF (closed stopband case). The frequency scanning range extends from 2.44 to 3.83 GHz. (a) Backward radiation patterns. (b) Forward radiation patterns.

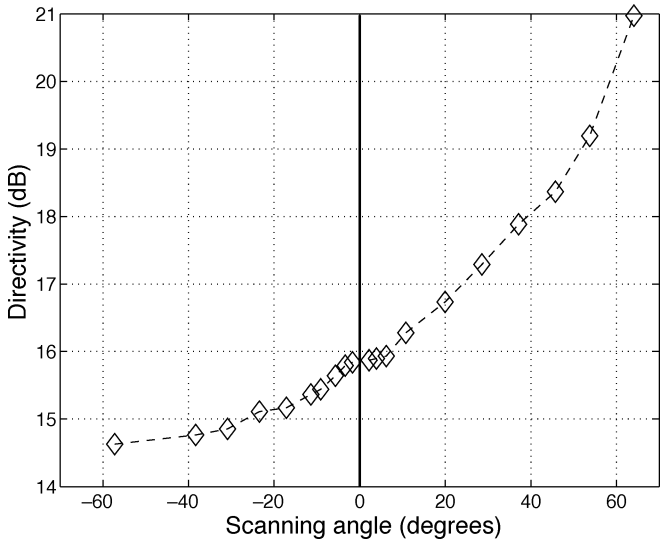

Fig. 21. Directivity of the loaded NRI-TL grid of [4], operating as an LWA, with loading elements $L_0 = 10.0$ nH and $C_0 = 1.0$ pF (closed stopband case).

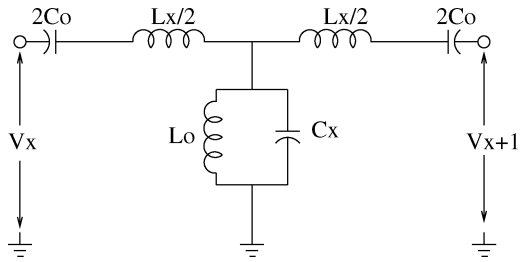

Fig. 22. Equivalent circuit representation of the lossless loaded NRI-TL metamaterial.

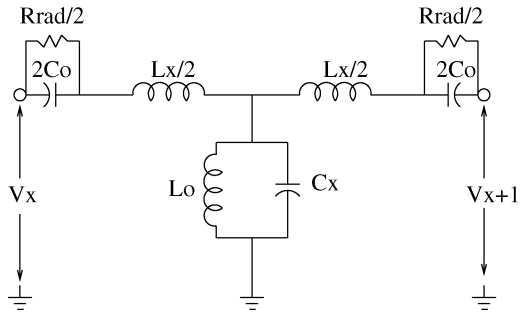

Fig. 23. Equivalent circuit representation of the lossless loaded NRI-TL metamaterial, accounting for radiation from the capacitive gaps of the grid.

with Floquet's theorem [23], [34]. However, the periodic analysis of the circuit of Fig. 22 can provide only purely real propagation constants for the supported modes (in the pass-band) or purely imaginary (in the stopband), as it involves only reactive components [23]. Therefore, this equivalent circuit cannot fully characterize a loaded NRI-TL metamaterial structure when it operates within its leaky-wave regime.

An alternative topology is shown in Fig. 23 [33]. It includes a resistor in parallel with the series capacitors which is aimed at representing radiation from the capacitive gaps. Nevertheless, a necessary condition for the periodic analysis of this circuit, in the sense of [23], is the determination of the value $R_{\rm rad}$ of this parallel resistor. To this end, a least-square-error (LSE) optimization procedure is followed, with an objective of minimizing the following expression:

$$\epsilon = \sum_i \left(a_i^{\text{eq. circuit}} - a_i^{\rm FDTD} \right)^2 \tag{8}$$

where $a_i^{\rm eq.circuit} = a^{\rm eq.circuit}(\omega_i)$ and $a_i^{\rm FDTD} = a^{\rm FDTD}(\omega_i)$ are the attenuation constants computed by the periodic analysis of the equivalent circuit of Fig. 23 and the periodic FDTD, respectively, at discrete frequencies ω_i within the fast-wave region

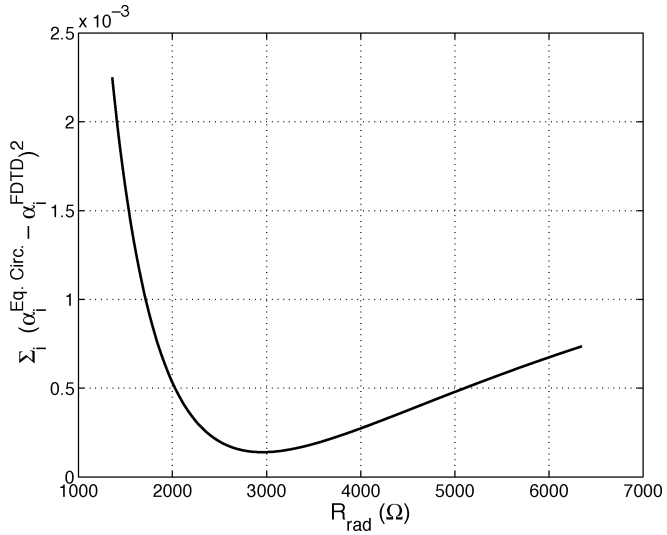

Fig. 24. Calculation of the resistor $R_{\rm rad}$ through the minimization of the squared error between the values of the attenuation constant calculated using the periodic FDTD analysis and the equivalent circuit.

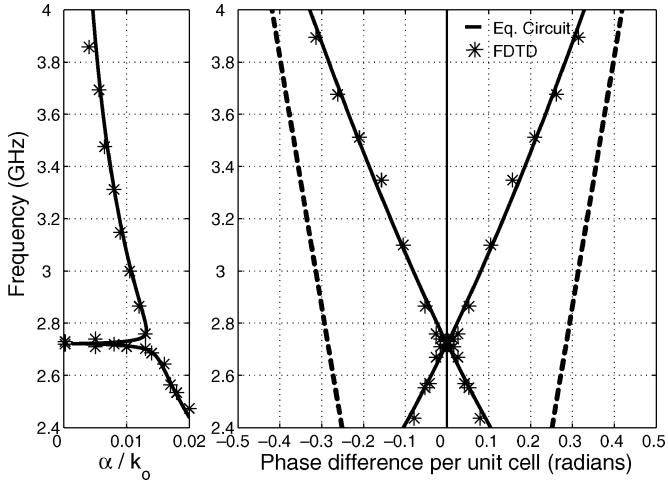

Fig. 25. Complex propagation constants of the radiating modes supported by the 2-D loaded NRI-TL grid of [4], operating as an LWA, with loading elements $L_0 = 10.0$ nH and $C_0 = 1.0$ pF (closed stopband case), calculated through the periodic analysis of the equivalent circuit of Fig. 23 and the periodic FDTD analysis. On the left, the attenuation constant is plotted as a function of frequency. On the right, the phase constant is plotted as a function of frequency (the dashed line indicates the light line $\beta = k_0$).

for the closed stopband case. This analysis, which is graphically demonstrated in Fig. 24, results in the value of $R_{\rm rad} = 2950\,\Omega$.

The dispersion diagram for the circuit of Fig. 23, using this value of the resistor, is compared to the FDTD results (for the closed stopband case) in Fig. 25. Evidently, the optimization of the value of $R_{\rm rad}$ in order to minimize the difference of the two methods with respect to the attenuation constant also ensured their agreement for the values of the phase constant.

Using the same value for $R_{\rm rad}$, the results of the equivalent circuit analysis and FDTD for the open stopband case are shown in Fig. 26. The two techniques agree well outside the stopband formed around the $\beta = 0$-point. However, the computation of modes by FDTD at the boundaries of and within the stopband is

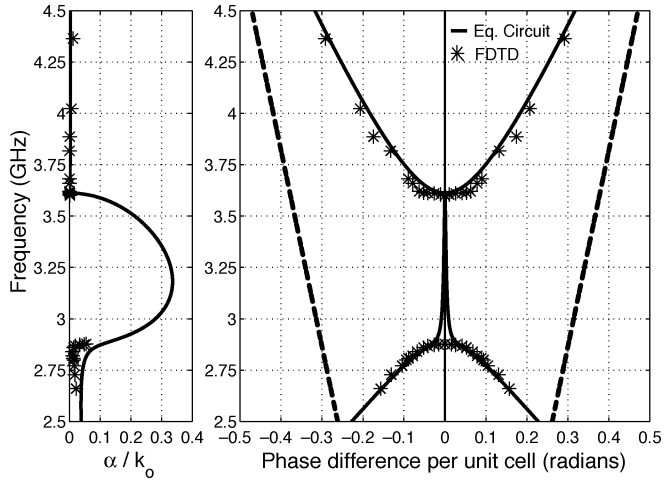

Fig. 26. Complex propagation constants of the radiating modes supported by the 2-D loaded NRI-TL grid of [4], operating as an LWA, with loading elements $L_0 = 5.6$ nH and $C_0 = 1.0$ pF (open stopband case), calculated through the periodic analysis of the equivalent circuit of Fig. 23 and the periodic FDTD analysis. On the left, the attenuation constant is plotted as a function of frequency. On the right, the phase constant is plotted as a function of frequency (dashed line indicates the light line $\beta = k_0$).

inhibited by the relatively large field attenuation associated with these modes that renders the field values sensitive to numerical errors. This effect is reflected on the observed deviation between FDTD and equivalent-circuit values of the attenuation constant α as the latter grows and the absence of FDTD results for α within the stopband.

B. Broadside Radiation From the 2-D Loaded NRI-TL Grid

The dispersion analysis results of Fig. 19, which refers to the closed stopband case, indicate that $\partial f/\partial\beta \to 0$, as $|\beta| \to 0$. As a result, the group velocity v_g is still zero at broadside (just as in the open stopband case), despite the implementation of the closed stopband condition. This implies that, *exactly* at broadside, the traveling wave ceases to propagate along the structure, and a standing wave, which is characterized by zero attenuation constant and group velocity, emerges. Clearly, this effect does not prevent the antenna from exhibiting a significant gain as $\beta \to 0^-$ and $\beta \to 0^+$ (Fig. 21). However, it is worth exploring this question further to obtain a complete understanding of this type of LWA. For this purpose, the equivalent circuit of the previous section is employed. Then, the dispersion diagram extracted from the periodic analysis of that circuit around $\beta = 0$ is shown in Fig. 27. Evidently, $v_g(\beta = 0) = 0$ in this case as well.

On the other hand, the possibility of the existence of a nonzero group velocity has been indicated in [9] and [10], based on [34], which pursues a periodic analysis of a *lossless* equivalent circuit similar to that of Fig. 22. However, the presence of radiating modes in a metamaterial grid has to be accounted for by the addition of a resistor to the corresponding equivalent circuit (also done in [32]). If this resistor is added as in Fig. 23, then the group velocity at broadside appears to be zero, which is in agreement with the FDTD results. Furthermore, the physical interpretation of the stopband closure condition of (7) is that it forces the resonance of the series capacitor with a $\beta d/2$ short-circuited section

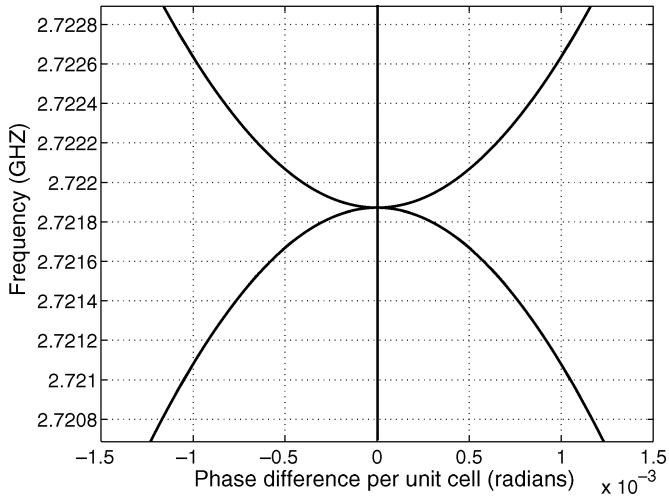

Fig. 27. Zoomed-in view of the Brillouin diagram of the 2-D loaded NRI-TL grid of [4] operating as an LWA with loading elements $L_0 = 10$ nH and $C_0 = 1.0$ pF (closed stopband case) calculated through the periodic analysis of the equivalent circuit of Fig. 23. The zero slope of the dispersion curve at $\beta = 0$ suggests that $v_g(\beta = 0) = 0$.

of the host TL to coincide with the resonance of the shunt inductor with a $\beta d/2$ open-circuited TL section [23]. These two resonances are responsible for the two edges of the stopband indicated around the $\beta = 0$-point in Fig. 16. Therefore, when these two coincide, the stopband closes. However, in the presence of the resistor, the matching (or "balancing") condition of (7) can only approximately assume this physical meaning and render the stopband exactly closed. In that case, while the stopband tends to close (and actually approaches this limit quite well, as shown in Fig. 19), the group velocity remains zero at $\beta = 0$. This perspective offers additional support to our FDTD and equivalent circuit results.

The behavior of the NRI-TL based LWA in this case presents an interesting similarity (in terms of the dependence of both the attenuation and the phase constant on frequency) with the periodic microstrip-based LWA structure proposed in [35], that radiated its $n = -1$ harmonic (as opposed to the fundamental harmonic, which is employed in the NRI-TL-based LWA). This structure also achieved almost continuous scanning through broadside and was inhibited only within a small stopband that occurred around the $\beta = 0$ point.

Finally, our conclusions do not contradict [34], since the latter totally omits the presence of losses, nor the experimental results of [9], since the possibility of achieving gain just before and right after broadside has also been suggested in Fig. 21. In fact, for all practical purposes, the ability of the NRI-TL LWA to achieve continuous scanning from backward to forward end-fire is confirmed by the results of this paper, despite the singular behavior of the $\beta = 0$ point.

VII. Conclusion

This paper showed that the extraction of attenuation constants of leaky waves excited in periodic structures *is* possible within the context of periodic FDTD analysis, according to a technique that was presented and validated. This technique offers an efficient alternative to the time-consuming conventional approach of approximating the behavior of infinite periodic structures by simulating truncated versions of those that are composed of sufficiently many unit cells. The validation of the proposed methodology led to its application to the modeling of metamaterial-based LWAs.

In particular, the leaky-wave operation of the 2-D NRI-TL medium of [4] was thoroughly investigated, and the frequency dependence of the directivity of this medium as a LWA, along with its radiation pattern, was provided for two representative cases. When the loading elements did not satisfy the condition (7), the directivity increased from backward end-fire until just before broadside, dropped to zero within the stopband formed in this case, and kept monotonically increasing after the stopband toward forward end-fire. On the other hand, when (7) was met, the directivity increased in a monotonic, almost continuous fashion from backward to forward end-fire, with the exception of the broadside direction.

Based on the FDTD results, a lumped-element equivalent circuit was extracted for this LWA. The periodic dispersion analysis of the circuit faithfully reproduced the FDTD results, accurately accounting for the radiation losses. Finally, the theoretically intriguing question of broadside radiation from the metamaterial grid was addressed by confirming that, although the grid can be designed to achieve almost continuous beam-scanning from backward to forward end-fire, exactly at broadside it seizes to support a traveling wave, due to the decay of the group velocity within the structure to zero at that point.

References

[1] V. G. Veselago, "The electrodynamics of substances with simultaneously negative values of ϵ and μ," *Sov. Phys.—USP*, vol. 10, pp. 509–514, 1968.

[2] D. R. Smith, W. J. Padilla, D. C. Vier, S. C. Nemat-Nasser, and S. Schultz, "Composite medium with simultaneously negative permeability and permittivity," *Phys. Rev. Lett.*, vol. 78, pp. 2933–2936, Oct. 2000.

[3] A. K. Iyer and G. V. Eleftheriades, "Negative refractive index metamaterials supporting 2-D waves," in *IEEE MTT-S Int. Microw. Symp. Dig.*, Seattle, WA, Jun. 2–7, 2002, pp. 1067–1070.

[4] G. V. Eleftheriades, A. K. Iyer, and P. C. Kremer, "Planar negative refractive index media using periodically loaded transmission lines," *IEEE Trans. Microw. Theory Tech.*, vol. 50, no. 12, pp. 2702–2712, Dec. 2002.

[5] C. Caloz and T. Itoh, "Application of the transmission line theory of left-handed (LH) materials to the realization of a microstrip LH transmission line," in *IEEE AP-S Int. Symp. Dig.*, Jun. 16–21, 2002, vol. 2, pp. 412–415.

[6] A. A. Oliner, "A periodic-structure negative-refractive-index medium without resonant elements," in *USNC/URSI Nat. Radio Sci. Meeting*, San Antonio, TX, Jun. 16–21, 2002, p. 41.

[7] A. Grbic and G. V. Eleftheriades, "A backward-wave antenna based on negative refractive index *L–C* networks," in *Proc. IEEE Int. Symp. Antennas Propag.*, San Antonio, TX, Jun. 16–21, 2002, vol. 4, pp. 340–343.

[8] ——, "Experimental verification of backward-wave radiation from a negative refractive index metamaterial," *J. Appl. Phys.*, vol. 92, no. 10, pp. 5930–5935, Nov. 2002.

[9] L. Liu, C. Caloz, and T. Itoh, "Dominant mode leaky-wave antenna with backfire-to-endfire scanning capability," *Electron. Lett.*, vol. 38, pp. 1414–1416, Nov. 2002.

[10] S. Lim, C. Caloz, and T. Itoh, "Metamaterial-based electronically controlled transmission-line structure as a novel leaky-wave antenna with tunable radiation angle and beamwidth," *IEEE Trans. Microw. Theory Tech.*, vol. 52, no. 12, pp. 2678–2690, Dec. 2004.

[11] A. K. Iyer and G. V. Eleftheriades, "Leaky-wave radiation from a two-dimensional NRI TL metamaterials," in *Proc. URSI Int. EM Theory Symp.*, May 2004, vol. 2, pp. 891–893.

[12] C. A. Allen, C. Caloz, and T. Itoh, "Leaky-waves in a metamaterial-based two-dimensional structure for a conical beam antenna application," in *IEEE MTT-S Int. Microw. Symp. Dig.*, Jun. 2004, vol. 3, pp. 305–308.
[13] A. K. Iyer and G. V. Eleftheriades, "Leaky-wave radiation from planar negative-refractive-index transmission-line metamaterials," in *Proc. IEEE Antennas Propag. Symp.*, Jun. 2004, vol. 2, pp. 1411–1414.
[14] P. Harms, R. Mittra, and W. Ko, "Implementation of the periodic boundary condition in the finite-difference time-domain algorithm for FSS structures," *IEEE Trans. Antennas Propag.*, vol. 42, no. 9, pp. 1317–1324, Sep. 1994.
[15] A. Taflove and S. Hagness, "Analysis of Periodic Structures," in *Computational Electrodynamics: The Finite Difference Time Domain Method*. Boston, MA: Artech House, 1995, ch. 13.
[16] M. Celuch-Marcysiak and W. K. Gwarek, "Spatially looped algorithms for time-domain analysis of periodic structures," *IEEE Trans. Microw. Theory Tech.*, vol. 43, no. 4, pp. 860–865, Apr. 1995.
[17] A. C. Cangellaris, M. Gribbons, and G. Sohos, "A hybrid spectral/FDTD method for the electromagnetic analysis of guided waves in periodic structures," *IEEE Microw. Guided Wave Lett.*, vol. 3, no. 10, pp. 375–377, Oct. 1993.
[18] T. Kokkinos, C. D. Sarris, and G. V. Eleftheriades, "Efficient finite-difference time-domain (FDTD) modeling of periodic leaky-wave structures," in *IEEE MTT-S Int. Microw. Symp. Dig.*, Jun. 2005, pp. 317–320.
[19] ——, "Finite-difference time-domain analysis of metamaterial-based leaky-wave antennas," in *IEEE AP-S Int. Symp. Dig.*, Jul. 2005, vol. 2A, pp. 26–29.
[20] M. Picket-May, B. Houshmand, and T. Itoh, "High speed electronic circuits with active and passive lumped elements," in *Computational Electrodynamics: The Finite Difference Time Domain Method*, A. Taflove and S. Hagness, Eds. Norwell, MA: Artech House, 1995, ch. 15.
[21] T. Kokkinos, C. D. Sarris, and G. V. Eleftheriades, "Periodic finite-difference time-domain analysis of loaded transmission-line negative-refractive-index metamaterials," *IEEE Trans. Microw. Theory Tech.*, vol. 53, no. 4, pp. 1488–1495, Apr. 2005.
[22] A. K. Iyer, P. C. Kremer, and G. V. Eleftheriades, "Experimental and theoretical verification of focusing in a large periodically loaded transmission line negative refractive index metamaterial," *Opt. Express*, vol. 11, pp. 696–708, Apr. 2003.
[23] A. Grbic and G. V. Eleftheriades, "Periodic analysis of a 2-D negative refractive index transmission line structure," *IEEE Trans. Antennas Propag.*, vol. 51, no. 10, pp. 2604–2611, Oct. 2003.
[24] L. Brillouin, *Wave Propagation in Periodic Structures: Electric Filters and Crystal Lattices*, 1st ed. New York: McGraw-Hill, 1946.
[25] G. C. Liang, Y. W. Liu, and K. K. Mei, "Full-wave analysis of coplanar waveguide and slotline using the time-domain finite-difference method," *IEEE Trans. Antennas Propag.*, vol. 53, no. 12, pp. 1845–1848, Dec. 1989.
[26] A. Grbic and G. Eleftheriades, "Leaky CPW-based slot antenna arrays for millimeter-wave applications," *IEEE Trans. Antennas Propag.*, vol. 50, no. 11, pp. 1494–1504, Nov. 2002.
[27] C. Caloz and T. Itoh, "Array factor approach of leaky-wave antennas and application to 1-D/2-D composite right/left-handed (CRLH) structures," *IEEE Microw. Wireless Compon. Lett.*, vol. 14, no. 6, pp. 274–276, Jun. 2004.
[28] K. L. Klohn, R. E. Horn, H. Jacobs, and E. Freibergs, "Silicon waveguide frequency scanning linear array antenna," *IEEE Trans. Microw. Theory Tech.*, vol. MTT-26, no. 10, pp. 764–773, Oct. 1978.
[29] M. Chen, B. Houshmand, and T. Itoh, "FDTD analysis of a metal-strip-loaded dielectric leaky-wave antenna," *IEEE Trans. Microw. Theory Tech.*, vol. 45, no. 8, pp. 1294–1301, Aug. 1997.
[30] A. Grbic and G. V. Eleftheriades, "Leaky CPW-based slot antenna arrays for millimeter-wave applications," *IEEE Trans. Antennas Propag.*, vol. 50, no. 11, pp. 1494–1504, Nov. 2002.
[31] G. V. Eleftheriades, O. Siddiqui, and A. K. Iyer, "Transmission line models for negative refractive index media and associated implementations without excess resonators," *IEEE Microw. Wireless Compon. Lett.*, vol. 13, no. 2, pp. 51–53, Feb. 2003.
[32] P. Burghignoli, G. Lovat, and D. R. Jackson, "Leaky-wave radiation at broadside from one-dimensional open periodic structures," in *Proc. IEEE Antennas Propag. Symp.*, , Jul. 2005, vol. 1B, pp. 264–267.
[33] G. V. Eleftheriades, A. Grbic, and A. K. Iyer, "Enabling electromagnetic applications of negative-refractive-index transmission-line metamaterials," in *Proc. Int. Antenna Technol. Appl. Electromagn. Symp.*, Ottawa, ON, Canada, Jul. 2004.
[34] A. Sanada, C. Caloz, and T. Itoh, "Characteristics of the composite right/left-handed transmission lines," *IEEE Microw. Wireless Compon. Lett.*, vol. 14, no. 2, pp. 68–70, Feb. 2004.
[35] P. Baccarelli, S. Paulotto, and D. R. Jackson, "Broadside radiation properties of 1D microstrip leaky-wave antennas," in *Proc. Int. Conf. Electromagn. Adv. Applicat.*, Turin, Italy, Sep. 12–16, 2005, pp. 755–758.

Titos Kokkinos (S'06) received the Diploma degree in electrical and computer engineering from the National Technical University of Athens (NTUA), Athens, Greece, in 2003, the M.A.Sc. degree in electrical and computer engineering from the University of Toronto, Toronto, ON, Canada, in 2005, and is currently working toward the Ph.D. degree in electronic and electrical engineering at Loughborough University, Loughborough, Leicestershire, U.K.

In 2001, he joined Siemens AG, Zürich, Switzerland. From May 2002 to June 2003, he was with the Optical Networking Group, NTUA, and from September 2003 to September 2005, he was with the Electromagnetics Group, University of Toronto. Since October 2005, he has been with the Wireless Communications Research Group, Loughborough University. His research interests include computational electromagnetics, NRI metamaterials, antennas design, microwave circuits design, and optical networks.

Costas D. Sarris (M'03) received the Diploma in electrical and computer engineering (with distinction) from the National Technical University of Athens (NTUA), Athens, Greece, in 1997, and the M.Sc. degree in electrical engineering, the M.Sc. degree in applied mathematics, and the Ph.D. degree from the University of Michigan, Ann Arbor, in 1998, 1998, and 2002, respectively.

In November 2002, he joined the Edward S. Rogers Sr. Department of Electrical and Computer Engineering, University of Toronto, Toronto, ON, Canada, where he is currently an Assistant Professor. His research interests are in the area of computational electromagnetics, with an emphasis on high-order, mesh-adaptive techniques. He is currently involved with basic research in novel numerical techniques, as well as applications of time-domain analysis to wireless channel modeling, wave propagation in complex media and meta-materials, and electromagnetic compatibility/interference (EMI/EMC) problems.

Prof. Sarris was the recipient of a number of scholarship distinctions, including the Hellenic Fellowship Foundation (1993–1997) and Technical Chamber of Greece (1994–1997) Awards for academic excellence and an NTUA 1997 Class Bronze Medal. He was the recipient of a Student Paper Award in the 2001 International Microwave Symposium for his work on a hybrid FDTD/MRTD numerical scheme and a Canada Foundation for Innovation New Opportunities Fund Award in 2004.

George V. Eleftheriades (S'86–M'88–SM'02–F'06) received the diploma (with distinction) from the National Technical University of Athens, Athens, Greece, in 1988, and the M.S.E.E. and Ph.D. degrees from the University of Michigan, Ann Arbor, in 1993 and 1989, respectively, all in electrical engineering.

During 1994–1997, he was with the Swiss Federal Institute of Technology, Lausanne, Switzerland, where he developed millimeter- and submillimeter-wave receiver technology for the European Space Agency and fast computer-aided design tools for planar packaged microwave circuits. In 1997, he joined the Edward S. Rogers Sr. Department of Electrical and Computer Engineering, University of Toronto, Toronto, ON, Canada, where he is now a Professor. He is leading a group of 15 graduate students in the areas of negative-refraction metamaterials and their microwave applications, integrated antennas and components for broad-band wireless telecommunications, novel antenna beam-steering techniques, low-loss silicon micromachined components, submillimeter-wave radiometric receivers, and electromagnetic design for high-speed digital circuits.

Prof. Eleftheriades was the recipient of the Gordon Slemon Award (teaching of design) from the University of Toronto and the Ontario Premier's Research Excellence Award, both in 2001. He was also the recipient of an E.W.R. Steacie Memorial Fellowship from the Natural Sciences and Engineering Research Council of Canada in 2004. Presently, he is an IEEE Distinguished Lecturer for the Antennas and Propagation Society.